



A free and open-source solution for Rietveld refinement of XRD data from the CheMin instrument onboard the Mars rover *Curiosity*



Nicola Döbelin^{a,*}, Richard Archer^{b,c}, Valerie Tu^d

^a RMS Foundation, Bischmattstrasse 12, 2544, Bettlach, Switzerland

^b Laboratory for Atmospheric and Space Physics, 1234 Innovation Drive, Boulder, CO, 80303, USA

^c NASA Johnson Space Center, 1601 NASA Parkway, Houston, TX, 77058, USA

^d Jacobs JETS at NASA Johnson Space Center, 1601 NASA Parkway, Houston, TX, 77058, USA

ARTICLE INFO

Keywords:

Mars rover *Curiosity*

CheMin

X-ray diffraction

Profex

Rietveld refinement

ABSTRACT

The Rietveld refinement software *Profex* is an open-source and platform-independent solution for the processing of powder X-ray diffraction datasets. It is based on the *BGMN* refinement kernel and uses a description of the diffractometer configuration to determine the instrument-related peak profile. In this article we present a *Profex* configuration file for the Chemistry and Mineralogy (CheMin) X-ray diffractometer (XRD), which is on-board the Mars Science Laboratory rover *Curiosity*. For the past decade, *Curiosity* has been on a mission on Mars to find out whether the planet was once habitable for microbial life. The CheMin XRD determines the mineralogical phases and abundances of Martian soil and rocks in Gale Crater, Mars. Since its arrival on Mars in 2012, *Curiosity* has analyzed powdered soil and rock samples with the CheMin instrument and transmitting the raw XRD data acquired back to Earth.

Adaptations of *Profex* to work seamlessly with CheMin XRD datasets involved creating a new configuration file for the CheMin instrument, as well as adding the Mars Mineral Compendium, a compilation of structural models specifically selected for the analysis of Mars sedimentary soil and rock samples, to *Profex*. Using example refinements, we demonstrate that this software solution is well suited for quantitative analysis of CheMin XRD datasets.

1. Introduction

Powder X-ray diffraction (XRD) is a technique widely used in mineralogy for the identification and quantification of crystalline phases in rock samples. However, powder diffraction patterns often suffer from severe peak overlap, making it challenging to distinguish distinct phases from one another. Difficulties in reconstructing the individual peaks and thus in determining reliable peak intensities were the reason why powder XRD was long considered to be of limited use for quantitative analyses. This changed in 1969, when H. Rietveld (1969) introduced a method for refining powder diffraction patterns that allowed the crystallographic parameters of crystal structure models to be fitted to a measured diffraction pattern. By evaluating the entire profile, the method is less susceptible to peak overlap than methods evaluating individual peaks. In addition to parameters of the crystal structure, the method also determines the quantitative proportions of the individual phases in phase mixtures (Madsen and Scarlett, 2008). Thus, the introduction of Rietveld

refinement also represented a milestone in the phase quantification of mineral samples. With the availability of affordable personal computers since the 1980s and their ever-increasing computational power, Rietveld refinement has become a standard tool for the analysis of crystalline samples and is still considered the most comprehensive method for the evaluation of powder XRD data.

After the publication of Rietveld's original algorithms for XRD profile generation, a variety of academic and commercial software implementations emerged. A directory of crystallographic software, including programs for Rietveld refinement, is maintained by the IUCr (IUCr, 2022). The Rietveld refinement kernel *BGMN* was developed by Bergmann et al. since the early 1990s (Bergmann et al., 1998). *BGMN* simulates the instrumental contribution to the peak profile from a description of the instrument's optical configuration and convolutes it with the wavelength distribution and refined sample-related profile parameters. This approach to profile generation is known as the fundamental parameters approach (FPA), and it eliminates the need to empirically

* Corresponding author.

E-mail address: nicola.doebelin@rms-foundation.ch (N. Döbelin).

<https://doi.org/10.1016/j.pss.2022.105596>

Received 5 August 2022; Received in revised form 26 October 2022; Accepted 29 October 2022

Available online 3 November 2022

0032-0633/© 2022 The Authors. Published by Elsevier Ltd. This is an open access article under the CC BY-NC-ND license (<http://creativecommons.org/licenses/by-nc-nd/4.0/>).

determine the instrument resolution function from a reference dataset (Bergmann et al., 2000). *BGMN* supports advanced anisotropic models for preferred orientation, crystallite size and micro-strain related peak broadening, as well as for thermal displacement parameters. A built-in interpreter language allows the user to program complex structure and task control files (Ufer et al., 2008). The user interacts with *BGMN* by editing input text files for task control and structure description, running the executables from the command line, and evaluating output text files. In 2013, N. Döbelin released a modern graphical user interface named *Profex* (Doebelin and Kleeberg, 2015), which was built around *BGMN* and greatly simplifies its use by supporting additional raw data file formats, providing text editors specifically for editing *BGMN* input files, and graphically displaying the refinement results. To extend the core functionality of *BGMN*, *Profex* contains modules for phase identification, conversion of CIF structure files to the *BGMN*-specific structure description format, creating electron density and difference Fourier maps, batch refinement, generic curve fitting, raw data manipulation, and various export formats for raw data, refinement results, and graphs. *Profex* is distributed as a free and open-source program for all major operating systems on the *Profex* website (Doebelin, 2022). The program is bundled with the *BGMN* Rietveld kernel, and a default set of structure models and configurations for laboratory instruments created by the author for his own use and contributed by *Profex* users are included.

The first crystallographic instrument to utilize XRD to analyze rocks and sediments on an extraterrestrial planet, was CheMin (Blake et al., 2021). Since then, no other flown mission has had an XRD onboard as part of the payload. Future missions, as summarized by Blake et al. (2021), would greatly benefit from having a definitive mineralogical instrument onboard. Here we provide a summary of some of the major mineralogical findings based on CheMin XRD analyses and refinements of the sediments and rocks of Gale crater, Mars.

Curiosity landed in Gale crater, Mars in August of 2012. At the time of writing this paper, *Curiosity* has spent a decade collecting data from the Martian surface. Analyses and refinement of the CheMin XRD data from sediments and rocks in Gale crater resulted in major mineralogical findings such as: 1) Tridymite and cristobalite, which are high temperature SiO_2 phases that might have formed by hydrothermal replacement processes (Morris et al., 2016) or by explosive silicic eruption (Payré et al., 2022); 2) Jarosite (Morris et al., 2016; Rampe et al., 2016, 2017), which is a mineral indicator of acidic conditions ($\text{pH} < 4$). Martin et al. (2017) constrain the age of jarosite with K–Ar dating to $\sim 2.1 \pm 0.4$ Ga; 3) Akaganeite, a chloride-containing iron(III) oxide-hydroxide mineral, which was hypothesized by Peretyazhko et al. (2016) to have formed in acid ($\text{pH} < 2$) microenvironments in Gale crater; 4) Ca-sulfate hydrations states as reported by Vaniman et al. (2014); 5) The presence of magnetite vs. hematite suggests changes to redox conditions in the lake waters or in later diagenetic fluids (Bristow et al., 2021; Hurowitz et al., 2017; Rampe et al., 2020, 2017); 6) Smectites that transitioned from trioctahedral to dioctahedral going up section in Gale crater (Bristow et al., 2018; Rampe et al., 2017; Tu et al., 2021). The refined unit cell parameters of these mineral phases in CheMin XRD data led to remarkable in-situ mineralogical discoveries of the environmental changes through time in Gale crater.

In this paper we present a new *Profex* instrument configuration for the CheMin diffractometer, which is installed onboard the Mars rover *Curiosity*, as well as a new collection of structure files specifically compiled for the evaluation of datasets collected on Mars. Using several examples, we demonstrate that these new additions to *Profex* can generate accurate Rietveld refinements and crystalline phase quantifications from CheMin datasets.

2. Materials and methods

2.1. CheMin instrument setup

Curiosity's main scientific mission goal was to study whether there is

evidence for past or present habitable environments for microbial life in Gale Crater, Mars. Its science payload, also known as the Mars Science Laboratory (MSL), carries 11 instruments to study the geology, atmosphere, environmental conditions, and potential biosignatures along the rover's traverse. The array of instruments includes multiple cameras, spectrometers, radiation detectors, and environmental and atmospheric sensors. CheMin is a combined XRD and X-ray fluorescence (XRF) instrument located inside the body of the rover. In addition to being the only X-ray diffractometer in space, CheMin is the first XRD instrument onboard any Mars exploration vehicle, which allowed a more definitive identification of minerals than any instrument used on previous missions because CheMin is capable of determining the crystal structure of mineral phases. CheMin collected 3 loose soil samples as well as 35 powdered rock samples, to date, obtained by drilling into the rock. Previously the CheMin instrument would deliver powdered or soil sediment to the instrument via ingestion into the Collection and Handling for In-Situ Martian Rock Analysis (CHIMRA) and sieved to a <150 μm grain size. A portion of the material was then deposited into CheMin's inlet funnel to deliver into a CheMin sample cell. Due to a malfunction with the drill feed motor, *Curiosity* now uses a method called “feed-extended drilling” or “feed-extended sample transfer” leaving the drill bit in the fully extended state (Fraeman et al., 2020) and the sample is delivered by hovering the drill bit over the inlet and is fed directly into CheMin using small amounts of reverse drill bit rotation and percussion.

The instrument setup of CheMin was presented in great detail by Blake et al. (2012). In brief, an X-ray tube with a Co anode generates a narrow parallel primary beam by means of a pinhole collimator. The sample material is held in a transmission geometry sample chamber and sonicated during data collection to convect the sample and improve particle statistics. A CCD detector is stationary on the opposite side of the sample (Fig. 1). This design is mechanically simple and allows great weight savings, as it requires few moving parts and no adjustable apertures. However, the detectable range of the diffraction angle is limited by the size and position of the detector. The raw data from the detector requires circular integration about the center of the 2D diffraction rings (Debye rings) and a geometric correction due to projection onto the flat detector surface to obtain a conventional one-dimensional diffraction pattern for evaluation by Rietveld refinement.

The CheMin team utilizes MDI JADE™ v9 (Materials Data Incorporated, Livermore, CA) software packages to perform Rietveld refinements on CheMin data to derive crystalline phases abundances (Rampe et al., 2017) and FULLPAT full pattern fitting method (Chiper and Bish, 2002) is used to derive abundances of phyllosilicate, poorly crystalline and XRD-amorphous phases. CheMin 1D diffraction patterns require offsets (-25 to -113 μm) applied to account for any differences in sample-to-detector distances when using different samples cells relative to an ideal sample cell-to-CCD distance of 18.5302 μm (Rampe et al., 2020). To correct for the offset, which results in a shift of the 2-theta peak position, an internal calibration method is used developed by Morrison et al. (2018) that is based on the refined unit cell parameters of plagioclase in most samples analyzed by CheMin.

A *Profex* instrument configuration file for CheMin was created using the graphical instrument editor. The X-ray source was specified as a micro-focus tube with a Co target of 50 μm in diameter. The tube was positioned 200 mm from the sample and a pinhole collimator with a 70 μm aperture was placed 10 mm from the sample. The sample chamber was configured as a transmission geometry cell with an aperture of 8 mm and a thickness of 1.10 mm. According to Blake et al. (2012), the true gap size was 175 μm . However, a configuration with a sample thickness of 175 μm produced a simulated peak profile that deviated greatly from the measured profile. The reason why a much larger sample thickness than the chamber gap size was necessary to describe the measured peak shape is not known, but could possibly be explained by bulging of the Kapton® or Mylar® windows during the measurements. The linear absorption coefficient of the sample for $\text{CoK}\alpha_1$ radiation was estimated at 63.2 cm^{-1} based on the refined composition of scooped soil sample “Rocknest”

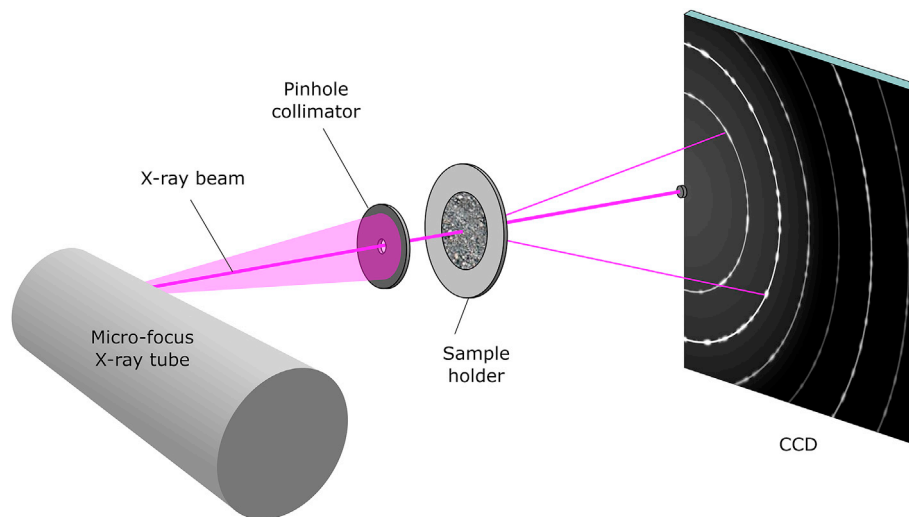


Fig. 1. Schematic representation of the CheMin instrument setup (adopted from Blake et al. (Blake et al., 2012)).

(example 1 in this study) and assuming a packing density of 33% while being sonicated in the sample chamber. The detector was configured as a point detector with an active area of one pixel ($40 \times 40 \mu\text{m}^2$). This was achieved by limiting the detector width to 0.040 mm and combining it with a detector slit with a height of 0.040 mm. This configuration accurately represented the effect of the true detector geometry on the integrated and geometrically corrected one-dimensional profile.

The emission spectrum for characteristic $\text{CoK}\alpha$ radiation was taken from Hölzer et al. (1997) using four Lorentzian curves to model the $\text{K}\alpha_1$ peak and three for $\text{K}\alpha_2$. An additional Lorentzian curve was added to model the residual $\text{K}\beta$ signal observed in CheMin datasets. Monte-Carlo simulation of the peak profile was performed at 8 distinct positions spread between 2.0 and $74.0^\circ 2\theta$, and interpolated profiles were calculated between 2.0 and $74.0^\circ 2\theta$ at a variable step size of $2 \cdot \sin(2\theta)$. All parameters for the BGMN instrument control file are listed in Table 1.

2.2. Mars Mineral Compendium

A suite of candidate Mars-relevant minerals, hereinafter referred to as the Mars Mineral Compendium, were compiled by Dr. Douglas W. Ming

(NASA Johnson Space Center) based on expected basalt mineral assemblages, and potential phases from the alteration of basalt. The intent of the compilation of mineral CIFs was to cover the breadth of elemental variability, however this is not an exhaustive list. The first edition of the Mars Mineral Compendium that was converted to the BGMN structure file format and bundled with Profex contained 241 structure models of 105 mineral phases. For many phases more than one structure model was included to account for chemical variations. We batch-converted the CIF files to the BGMN structure file format with the structure import function in Profex. The converted files were then manually revised and edited to use consistent file, phase, and goal names, references to the data sources were completed, and default settings for refined parameters were adjusted by disabling the refinement of preferred orientation and micro-strain, and by setting the refinement of crystallite-size related peak broadening to isotropic. Literal duplicates within the Mars Mineral Compendium were removed, but duplications with the standard Profex and BGMN structure collections, which were also included in the Profex distribution packages, were kept. The edited collection contained minerals relevant to Mars which included: feldspars (9), iron oxides and hydroxides (10), pyroxenes (13), SiO_2 phases (4), phyllosilicates (21), sulphates and sulphides (21), chlorates and chlorides (14), phosphates and phosphides (5), as well as 8 minerals from other groups such as carbonates and zeolites.

2.3. Application

XRD datasets acquired by CheMin on Mars are publicly available from the Open Data Repository (ODR) (Open Data Repository, 2022). The Profex instrument configuration for CheMin was tested by refining several example datasets and by analyzing the quality of the fit (Table 2). Sampling localities are shown in Fig. 2, descriptions of the localities were taken from the ODR records. The one-dimensional datasets retrieved from the ODR were previously integrated and corrected for geometric distortion. The data was provided as text files which could be opened in Profex either using the “Comma separated values” input file format or by dragging and dropping the file on the Profex main window. However, since the data files do not contain any information about the wavelength used by CheMin and Profex assumes $\text{CuK}\alpha$ radiation by default, the wavelength was manually changed to $\text{CoK}\alpha$ in the menu “Project → set project wavelength”. Once a refinement project had been created using the CheMin instrument configuration, the correct $\text{CoK}\alpha$ wavelength was applied regardless of previous settings. Major phases were identified by double-clicking the strongest unassigned peak, but later in the process the search-match module was used to identify phases with weaker

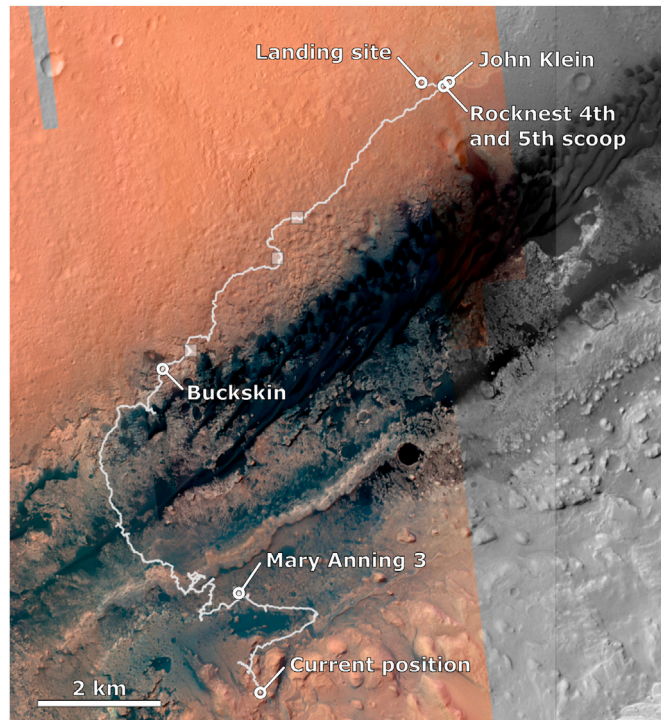
Table 1
BGMN instrument control parameters for CheMin. All distances are given in mm.

Variable	Value	Description
GEOMETRY	TRANSMISSION	Diffraction geometry
R	200	Diffractometer radius
FocusH	0.05	Axial tube focus width
FocusW	0.05	Apparent equatorial tube focus height
RoundListR	10.0	Distance of the pinhole aperture from the sample
RoundSlitD	0.07	Diameter of the pinhole aperture
SamplD	8.0	Diameter of the sample chamber
T	1.10	Sample thickness
D	0.1582	Reciprocal linear absorption coefficient (1/LAC) in mm
DetW	0.04	Equatorial opening of the detector slit
DetH	0.04	Axial width of the detector
zweiTheta[1] ... [8]	2, 5, 12, 21, 32, 45, 59, 74	Positions in 2θ for Monte-Carlo profile simulation
WMIN	2	Lower limit in 2θ for profile interpolation
WMAX	74	Upper limit in 2θ for profile interpolation
WSTEP	$2 \cdot \sin(2 \cdot \text{acos}(0))$ $\cdot \text{zweiTheta}/180$	Step size for profile interpolation in 2θ ($2 \cdot \text{acos}(0) = \pi$)

Table 2

Descriptions of ODR datasets used to verify the CheMin instrument configuration for Profex.

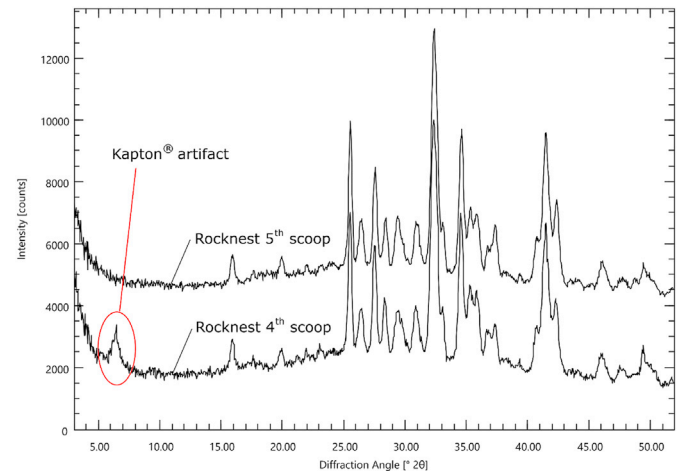
Analysis ID	XRD Product ID	Sols of analysis	CheMin cell
“Rocknest” 4th scoop	CMA_404470826RDA00790050104CH11503P1	78–87	1a Kapton
“Rocknest” 5th scoop	CMA_405889312RDA00950050104CH11504P1	94–119	7a Mylar
“John Klein A”	CMA_414856883RDA01960060000CH12240P1	196–269	13b Mylar
“John Klein B”	CMA_414856883RDA01960060000CH12240P2	196–273	13b Mylar
“John Klein C”	CMB_439549561RDA04740240192CH00111P1	473–488	13b Mylar
“Buckskin”	CMB_491748904RDA10620482542CH00111P1	1061–1078	14b Kapton
“Mary Anning 3”	CMB_653942038MIN28880822176CH00111P1	2888–2894	7a mylar

**Fig. 2.** The sampling locations of the example datasets processed in this article are spread along Curiosity's route. Map data courtesy of NASA, July 18, 2022.

signals. Search-match was limited to the Mars Mineral Compendium.

The CheMin sample wheel is equipped with sample cells using either Kapton® or Mylar® windows. A comparison of examples “Rocknest” 4th and 5th scoop, which used Kapton® and Mylar® windows, respectively, showed that the Kapton® foil produced a peak at 6.4° 2 θ (Fig. 3). To avoid misfits due to this artefact, all datasets were clipped at 8°–52° 2 θ for Rietveld refinement, unless mentioned otherwise.

A similar refinement strategy was followed for all example projects. If available, structure files from the Mars Mineral Compendium were used, otherwise those from the default “Minerals” repository included in Profex were used. No zero-point or sample displacement was refined, and crystallite sizes were refined isotropically. Isotropic micro-strain was only refined if an improvement of the fit was evident. Refinement of preferred orientation was disabled for phases less than 20 wt%. For phases with a quantity greater than 20 wt%, preferred orientation was refined with a spherical harmonics model of the second order to account for orientation in the crystallographic direction corresponding to the predominant crystal faces. Preferred orientation of the strongest phase was refined with a spherical harmonics function matched to the phase's characteristic crystal morphology and cleavage. In general, only moderate preferred orientation was expected based on the design of the sample chamber. No atomic site parameters were refined in any of the examples. The number of background polynomial coefficients was selected automatically.

**Fig. 3.** The Kapton® windows used with the “Rocknest” 4th scoop sample cell produced a peak at 6.4° 2 θ which was absent when a Mylar® window was used (“Rocknest” 5th scoop).

The quality of refinement from CheMin XRD datasets are the focus of this paper and here we report on the results from the refinements using Profex on four examples of CheMin samples. These specific CheMin datasets were chosen as examples to demonstrate the versatility and breadth of Profex to refine data representing differences in mineralogy, lithology, grain motion, and acquisition parameters. More specifically, “Rocknest” 4th and 5th scoops were selected to compare the effect of the Mylar® and Kapton® foils on the signal quality. The “John Klein” sample was selected because three different datasets with different acquisition times were deposited in the ODR, which allowed us to compare the effect of raw data quality on the refinement results. The “Buckskin” and “Mary Anning 3” samples were selected because their mineralogical composition differed from the previous samples, and because their locations covered a wide range of Curiosity's traverse.

3. Results

3.1. Example: “Rocknest” 4th and 5th scoop

Curiosity collected several scoops of loose, unconsolidated material from an aeolian sand shadow at the “Rocknest” location. Scoops 3 and 4 were combined in CheMin's cell 1a and are referred to as the 4th scoop, and scoop 5 was delivered to cell 7a, a pristine Mylar cell (Fig. 4).

The main phases were identified from the plagioclase, olivine, and pyroxene mineral groups. For the refinement project, the phases labradorite, forsterite, augite, and pigeonite were selected based on the closest matching peak positions. Signals of ilmenite and quartz were clearly detected, whereas the signals of hematite and magnetite were not clearly recognizable. After the first run of the Rietveld refinement, the default limits for refined cell parameter of the feldspar and pyroxene phases were found to be too strict. In order to account for the chemical variability of these phase systems, the limits were increased manually until a stable

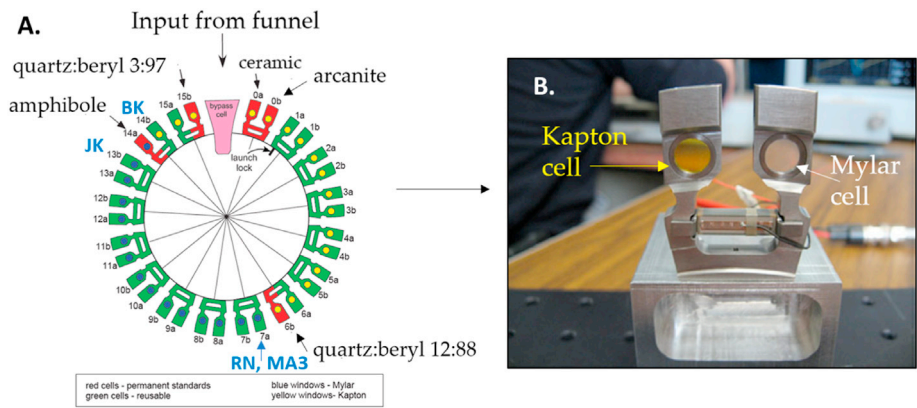


Fig. 4. (A) CheMin sample wheel that contains 27 reusable samples (green) and 5 standards (red) and the samples chosen for this demonstration (blue font): “Rocknest” (RN), “Mary Anning 3” (MA3), “John Klein” (JK), and “Buckskin” (BK). (B) An example of the CheMin sample cells with Kapton cell (yellow window) and Mylar cell (clear window). The figure was adopted from Blake et al. (Blake et al., 2012).

convergence was observed. For the last cycle, the refinement strategy provided in Table 3 was used. Based on the two cleavages of plagioclase (perfect and good), preferred orientation of labradorite phase was refined with a spherical harmonics model of the fourth order.

An underestimation of the labradorite $d(1-10)$ peak at 15.90° was observed in both datasets, possibly due to an inaccurate representation of the true feldspar composition in the selected labradorite structure. The refined phase quantities are listed in Table 4 and refinement statistics are given in Table 5. The refined patterns in Fig. 5 show a good agreement of the calculated and measured patterns, with deviations generally being close to the counting noise amplitude. In the summary tables we refer to the labradorite phase more generically as plagioclase to account for the fact that the selected structure model not necessarily represented the true plagioclase composition.

Comparing the outcome of the refinement with *Profex* with the phase quantities taken from the ODR (Table 4) shows that there are differences in both phase identification and quantification. We found low amounts of hematite and ilmenite in both samples, whereas according to the ODR these phases were only found in scoop 5. The ODR also lists anhydrite in both samples and sanidine in scoop 5. Neither of the two phases were detected with *Profex*. Some systematic differences between *Profex* and ODR phase quantities were observed. With *Profex* we found less plagioclase but more forsterite in both samples. The sums of the two pyroxenes augite and pigeonite were in very good agreement, but the individual quantities differed strongly between *Profex* and the ODR. The remaining phases were all quantified as <3.0 wt%.

3.2. Example: “John Klein”

The “John Klein” sample was the second sample collected by MSL and was drilled in the Yellowknife Bay formation, Sheepbed mudstone member (Vaniman et al., 2014) and is interpreted to be a shallow

Table 4
Refined phase quantities of “Rocknest” 4th and 5th scoop in relative wt.%. Errors represent the twice the estimated standard deviations (2 ESD) reported by BGMN. For comparison, the refined quantities reported in the ODR are shown as well. Values below 3-sigma are shown in parentheses.

Phase	“Rocknest” 4 th scoop		“Rocknest” 5 th scoop	
	<i>Profex</i>	ODR	<i>Profex</i>	ODR
Plagioclase	43.5 ± 1.6	45.8 ± 4.5	37.5 ± 1.3	40.8 ± 2.4
Forsterite	21.9 ± 1.1	18.2 ± 2.6	28.6 ± 0.9	22.4 ± 1.9
Augite	22.4 ± 2.0	18.1 ± 3.8	23.4 ± 1.5	14.6 ± 2.8
Pigeonite	6.4 ± 1.1	11.4 ± 4.1	5.5 ± 1.0	13.8 ± 2.8
Hematite	1.4 ± 0.2	–	1.2 ± 0.2	(1.1 ± 0.9)
Magnetite	1.2 ± 0.6	2.7 ± 1.0	0.3 ± 0.2	2.1 ± 0.8
Ilmenite	1.3 ± 0.2	–	1.3 ± 0.2	(0.9 ± 0.9)
Quartz	1.8 ± 0.3	1.6 ± 0.7	2.3 ± 0.3	1.4 ± 0.6
Anhydrite	–	2.1 ± 0.7	–	1.5 ± 0.7
Sanidine	–	–	–	(1.3 ± 1.3)

Table 5
Goodness of fit and refinement statistics of the “Rocknest” 4th and 5th scoop Rietveld refinements.

Parameter	“Rocknest” 4 th scoop	“Rocknest” 5 th scoop
R_{wp}	4.37%	3.80%
R_{exp}	1.89%	1.94%
χ^2	5.35	3.84
Number of refined peaks	219	219
Number of refined parameters	74	74
Number of background coefficients	9	9

lacustrine deposit (Grotzinger et al., 2014). Dataset “John Klein A” was a preliminary analysis measured from sol 196 to sol 269. More frames were

Table 3
Refinement strategy for both “Rocknest” datasets. Isotropically refined parameters are marked with “+”, fixed ones with “0”. Anisotropically refined parameters are marked with “++”. Preferred orientation refined with a spherical harmonics function is marked with “SPHARn”, where n stands for the order of the function. If a parameter did not converge to a minimum and was blocked by a manually set limit, it is marked by parentheses “()”. “Atomic sites” refers to site occupancies, fractional coordinates, and thermal displacement parameters.

Phase	Cell parameters	Scale factor	Crystallite size	Micro-strain	Preferred orientation	Atomic sites
Plagioclase	+	+	+	+	SPHAR4	0
Forsterite	+	+	+	0	SPHAR2	0
Augite	+	+	+	0	SPHAR2	0
Pigeonite	+	+	+	0	0	0
Hematite	+	+	(+)	0	0	0
Magnetite	+	+	+	0	0	0
Ilmenite	+	+	(+)	0	0	0
Quartz	+	+	+	0	0	0

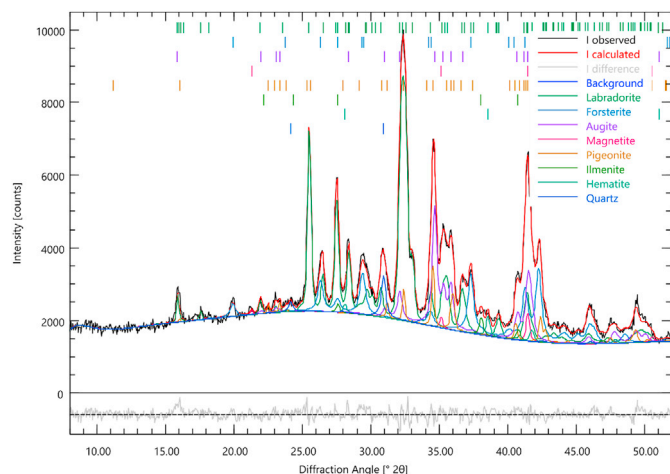


Fig. 5. Refined dataset of “Rocknest” 4th scoop. A similar quality of fit was obtained with “Rocknest” 5th scoop.

acquired for “John Klein B” from sol 270 to sol 273 and merged with the data of “John Klein A”. Later, the sample was reanalyzed from sol 473 to sol 488 (“John Klein C”) as part of a dehydration experiment within the CheMin sample cell (Vaniman et al., 2014).

We found a relatively complex mineralogical composition with 14 crystalline phases. The refinement strategy shown in Table 6 was used for all three samples. From the plagioclase group, andesine and labradorite closely matched the measured peak positions and intensities. Based on the slightly better match of the peak duplet near 18° 2θ, andesine was selected over labradorite. Andesine was the only phase that resulted in >20 wt% phase quantity and was therefore the only phase for which preferred orientation was refined with a spherical harmonics function of the fourth order. A weak signal of sanidine was observed, and the best match of the peaks positions was obtained with composition $\text{Na}_{0.35}\text{K}_{0.65}\text{AlSi}_3\text{O}_8$. Due to the low signal definition and severe peak overlap, crystallite-size related peak broadening could not be refined reliably and had to be limited manually.

The signals of all pyroxene phases were clearly visible and the phase quantifications were surprisingly stable and reproducible despite similar peak positions. The fact that no preferred orientation and no anisotropic peak broadening were refined for all three pyroxenes contributed to the stability of the refinement.

The magnetite signal was well defined, and even though the strongest $d(311)$ peak at 41.45° 2θ overlapped with peaks of andesine, ferrosilite, augite, and forsterite, other peaks were well separated and resulted in a

robust refinement. The hematite signal was much weaker, but the $d(114)$ peak at 38.55° 2θ was unobscured and allowed unambiguous identification of the phase. Accordingly, forsterite, anhydrite, and bassanite all had at least one unobscured peak that allowed the phase to be identified and quantified. Akaganeite was added to fit a duplet of peaks at 13.8° 2θ. Weak residual signals were assigned to gypsum and rozenite ($\text{FeSO}_4 \cdot 4\text{H}_2\text{O}$), but the identification was not conclusive. Both phases had to be restricted in crystallite-size related peak broadening to avoid excessive broadening leading to strong correlation of the phase quantity with the background intensity.

A broad peak was observed at 10.0° 2θ. To facilitate stable refinement of this peak and the background polynomial, the dataset was clipped at 7.0° 2θ instead of 8.0° 2θ to include background signal on both sides of the peak. Prior to adjusting the lower clipping angle, it was verified that no diffraction data was evident at or below 7.0° 2θ. The $d(001)$ peaks of several mica phases matched the position at 10.0° 2θ, including biotite, muscovite, phlogopite, zinnwaldite, and annite, but the lowest χ^2 value was obtained with biotite. Crystallite-size related peak broadening had to be restricted manually because with the exception of the $d(001)$ peak, all

Table 7

Refined phase quantities of “John Klein” samples in relative wt.%. Profex quantities are normalized to the sum of all refined phases excluding biotite for comparison with ODR results. Errors of sample quantities represent twice the estimated standard deviations (2 ESD) reported by BGMN. For comparison, the refined quantities of sample A reported in the ODR are shown as well. Values below 3-sigma are shown in parentheses.

Phase	“John Klein A”		“John Klein B”		“John Klein C”
	Profex	ODR	Profex	Profex	Profex
Plagioclase	33.2 ± 0.7	43.8 ± 3.6	30.8 ± 1.0		32.6 ± 1.0
Sanidine	2.9 ± 0.3	(1.7 ± 1.8)	0.8 ± 0.4		0.9 ± 0.3
Forsterite	8.6 ± 0.8	5.1 ± 3.3	6.0 ± 0.7		8.3 ± 0.6
Ferrosilite	13.7 ± 1.2	6.8 ± 3.1	19.7 ± 1.3		13.8 ± 1.0
Pigeonite	8.7 ± 1.0	12.7 ± 4.0	8.7 ± 0.9		7.9 ± 0.8
Augite	11.0 ± 0.9	8.5 ± 3.4	12.0 ± 1.2		17.6 ± 0.9
Hematite	2.2 ± 0.3	(1.2 ± 0.9)	1.3 ± 0.3		1.4 ± 0.2
Magnetite	7.0 ± 0.4	7.0 ± 1.9	5.7 ± 0.5		6.0 ± 0.3
Anhydrite	6.2 ± 0.3	3.3 ± 2.1	7.3 ± 0.3		5.5 ± 0.3
Bassanite	1.8 ± 0.2	2.0 ± 0.9	2.3 ± 0.2		1.7 ± 0.2
Akaganeite	0.9 ± 0.2	2.4 ± 1.4	1.3 ± 0.1		0.5 ± 0.1
Gypsum	1.9 ± 0.2	–	2.1 ± 0.2		2.0 ± 0.2
Rozenite	1.8 ± 0.2	–	2.1 ± 0.2		1.6 ± 0.2
Biotite	+8.8 ± 0.5	–	+10.0 ± 0.5		+8.1 ± 0.4
Albite	–	2.7 ± 1.3	–		–
Quartz	–	(0.6 ± 0.7)	–		–
Halite	–	(0.2 ± 0.3)	–		–
Pyrite	–	(0.4 ± 0.5)	–		–
Pyrrhotite	–	(1.5 ± 1.5)	–		–

Table 6

Refinement strategy for all “John Klein” datasets. Isotropically refined parameters are marked with “+”, fixed ones with “0”. Anisotropically refined parameters are marked with “++”. Preferred orientation refined with a spherical harmonics function is marked with “SPHARn”, where n stands for the order of the function. If a parameter did not converge to a minimum and was blocked by a manually set limit, it is marked by parentheses “()”. “Atomic sites” refers to site occupancies, fractional coordinates, and thermal displacement parameters.

Phase	Cell parameters	Scale factor	Crystallite size	Micro-strain	Preferred orientation	Atomic sites
Plagioclase	+	+	+	+	SPHAR4	0
Sanidine	+	+	(+)	0	0	0
Forsterite	+	+	+	0	0	0
Ferrosilite	+	+	+	0	0	0
Pigeonite	+	+	+	0	0	0
Augite	+	+	+	0	0	0
Hematite	+	+	+	0	0	0
Magnetite	+	+	+	0	0	0
Biotite	+	+	(+)	0	0	0
Anhydrite	+	+	+	0	0	0
Bassanite	+	+	+	0	0	0
Gypsum	+	+	(+)	0	0	0
Rozenite	+	+	(+)	0	0	0
Akaganeite	+	+	(+)	0	0	0

other peaks strongly overlapped with other phases.

Refined phase quantities (Table 7) showed relatively good agreement among the three datasets. Since the quantities obtained from the ODR excluded phyllosilicates, our quantities presented in Table 7 were normalized to the sum of all phases excluding biotite, and biotite was reported in addition. Major components of the sample were plagioclase and pyroxenes, each group accounting for 30–40 wt%. The quality of fit parameters presented in Table 8 and the example refinement shown in Fig. 6 demonstrate again an accurate description of the peak profiles by *Profex*'s CheMin instrument configuration. The background polynomial with 9 coefficients, as automatically selected by *BGMN*, could follow the background also at low angles. The systematic residual signals did not exceed the counting noise as observed in the difference curves. However, the ambiguous identification and quantification of gypsum, rozenite, and biotite exposed the limits of phase detection from CheMin datasets of the given complexity.

A comparison with the phase identification of dataset “John Klein A” taken from the ODR shows again differences in interpretation of signals near the detection limit (Table 7). We were unable to reproduce the results of the ODR which suggest the presence of albite, quartz, halite, pyrite, and pyrrhotite. In addition, the identification of gypsum and rozenite was unconfirmed due to signal ambiguity. Substantial differences were found in the quantifications of plagioclase, ferrosilite, pigeonite, and augite due to strong peak overlap, making specific phases difficult to distinguish.

3.3. Example: “Buckskin”

When exploring the Marias Pass region on lower Mount Sharp, *Curiosity* drilled a hole in a rock target called “Buckskin”. CheMin collected 15 minor frames of the drill material, of which only the first four produced smooth diffraction signals (Morris et al., 2016; Rampe et al., 2017). The last eleven produced spotty Debye 2D diffraction rings, possibly due to packing of the sample which may have prevented grain motion by sonication. The dataset analyzed here represents 2 h of analysis from the first four frames combined.

Other than the previous examples, we found a very pronounced signal of low-temperature tridymite (SiO_2) in the monoclinic space group $C1c1$ in the “Buckskin” sample. This observation was in agreement with the phase composition recently reported by Payré et al. (2022). The second major component was identified as a plagioclase feldspar of intermediate composition, closely matching the peak positions of labradorite. Magnetite was clearly identified, but no hematite was found. Only traces of pigeonite were detected, thus “Buckskin” was largely free of pyroxenes. Anhydrite, bassanite, and sanidine were identified based on a few peaks of low intensity, typically 2–3 times higher than the noise amplitude.

The refinement strategy shown in Table 9 was used to determine the phase abundances. The quantities of the two phases, low tridymite and labradorite, were >20 wt%. Both phases were therefore refined with a fourth order preferred orientation model (SPHAR4) to account for the two directions of cleavage (plagioclase: perfect and good, tridymite: indistinct and imperfect). However, before enabling this feature for two

Table 8

Goodness of fit and refinement statistics of the “John Klein” Rietveld refinements.

Parameter	“John Klein A”	“John Klein B”	“John Klein C”
R_{wp}	4.54%	3.62%	3.84%
R_{exp}	1.94%	2.01%	2.14%
χ^2	5.48	3.24	3.22
Number of refined peaks	583	583	583
Number of refined parameters	93	93	93
Number of background coefficients	9	9	9

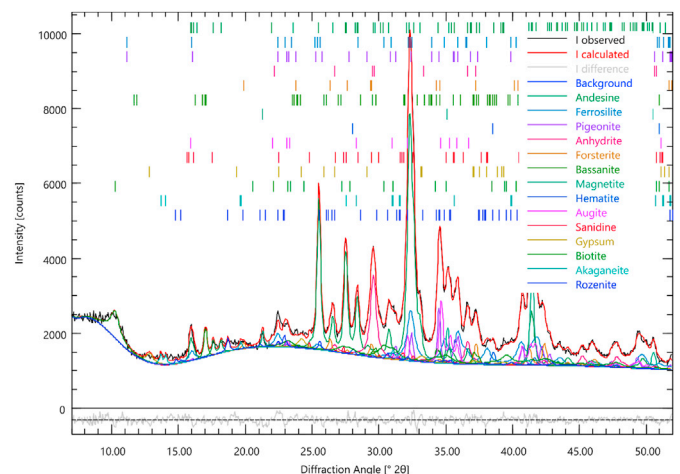


Fig. 6. Refinement of sample “John Klein B”. The quality of fit is representative for all “John Klein” datasets.

phases, we verified that no excessive peak overlap occurred among them. The *BGMN* Rietveld kernel checks for sufficiently good data quality before enabling texture refinement. The signal-to-noise ratio of low tridymite and labradorite was deemed insufficient for a spherical harmonics function of the fourth order and was thus reduced to a second order model (SPHAR2) by the refinement kernel. Hence, although we specified a fourth order preferred orientation function in the structure models of both phases, they were effectively refined with second order functions.

The refinement converged with $\chi^2 = 0.46$ (Table 10), which indicated insufficient signal-to-noise ratio for the refined number of parameters. Indeed, the peak intensities were lower than in previous datasets (Fig. 7) due to the data acquisition time limited to only 2 h. The default limits of cell parameters and peak broadening parameters were too strict for some phases, but after increasing them, all refined parameters reached a stable minimum.

Phase quantification (Table 11) confirmed that the sample mainly comprised low tridymite and plagioclase (labradorite), followed by magnetite, sanidine, and pyroxene (pigeonite). Calcium sulphates were observed near the detection limit. The estimated standard deviations (ESD) reported by the refinement kernel were substantially greater than in previous examples, most likely due to the lower signal-to-noise ratio. The difference curve did not show any residual signals above the noise amplitude. Quantification of the strong phases tridymite, plagioclase, sanidine, and magnetite were in very strong agreement with the results obtained from the ODR. Differences in phase identification were again limited to weak signals of pigeonite, bassanite, and cristobalite.

3.4. Example: “Mary Anning 3”

A relatively recent dataset found in the ODR database at the time of writing this article was collected from the “Mary Anning 3” drill site and analyzed by CheMin from sols 2888 to 2894. 45 minor frames were measured, representing a total acquisition time of 22.5 h.

The “Mary Anning 3” dataset proved challenging to identify phases and refine unit cell parameters and phase quantities because phase identification with *Profex* resulted in a large number of phases and inconclusive assignment of a group of low-angle peaks. The main phase was easily identified as the well-known plagioclase, best matched by a labradorite structure. Other phases already known from the previous examples included pyroxene (matched by pigeonite), the sulphates bassanite, anhydrite, and rozenite, as well as quartz. The new phases siderite and goethite were also easily identified. However, a group of peaks between 9° and 12° 2θ with a basal d -spacing of 10 \AA indicated the presence of phyllosilicates. The group consisted of a sharp peak at 11.0° 2θ , which

Table 9

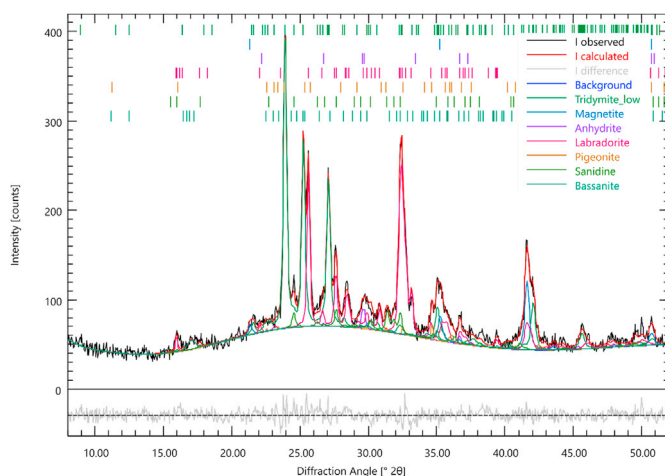
Refinement strategy for the “Buckskin” dataset. Isotropically refined parameters are marked with “+”, fixed ones with “0”. Anisotropically refined parameters are marked with “++”. Preferred orientation refined with a spherical harmonics function is marked with “SPHARn”, where n stands for the order of the function. If a parameter did not converge to a minimum and was blocked by a manually set limit, it is marked by parentheses “()”. “Atomic sites” refers to site occupancies, fractional coordinates, and thermal displacement parameters.

Phase	Cell parameters	Scale factor	Crystallite size	Micro-strain	Preferred orientation	Atomic sites
Tridymite low	+	+	+	+	SPHAR4	0
Plagioclase	+	+	+	+	SPHAR4	0
Sanidine	+	+	+	0	0	0
Pigeonite	+	+	+	0	0	0
Magnetite	+	+	+	0	0	0
Anhydrite	+	+	+	0	0	0
Bassanite	+	+	+	0	0	0

Table 10

Goodness of fit and refinement statistics of the “Buckskin” Rietveld refinement.

Parameter	Value
R_{wp}	7.60%
R_{exp}	11.19%
χ^2	0.46
Number of refined peaks	425
Number of refined parameters	61
Number of background coefficients	9

**Fig. 7.** Refinement of the “Buckskin” sample.**Table 11**

Refined phase quantities of the “Buckskin” sample in relative wt.%. Errors of sample quantities represent twice the estimated standard deviations (2 ESD) reported by BGMN. For comparison, the refined quantities of sample A reported in the ODR are shown as well.

Phase	“Buckskin”	
	Profex	ODR
Tridymite low	33.8 ± 2.4	34.1 ± 2.0
Plagioclase	42.7 ± 3.8	42.8 ± 3.0
Sanidine	7.8 ± 3.4	8.4 ± 1.8
Pigeonite	2.2 ± 1.3	–
Magnetite	9.0 ± 2.0	6.9 ± 0.8
Anhydrite	1.6 ± 1.0	1.8 ± 0.6
Bassanite	3.0 ± 1.3	–
Cristobalite	–	6.0 ± 0.8

was assigned to pyrophyllite-1A in space group *P*-1, and a broad signal between 9.5° and 11.7° 2θ, of which it was unclear whether it represented a single broad peak or several peaks of medium width. Eventually, it was decided to assign the two phases biotite and muscovite, assuming

that the broad signal represented the overlapping peaks *d*(001) of biotite and *d*(002) of muscovite. A broad increase of intensity starting at 22.5° 2θ and dragged out towards higher angles was also observed. The BGMN structure collection included with Profex contains a model created by Ufer et al. (2008) for a turbostratically disordered smectite structure. This structure with file name “smectitedi2wfix.str” described the signal starting at 22.5° 2θ and fading towards higher angles relatively accurately, therefore we decided to add it to the refinement project. Rozenite was added to fit a very broad peak centered at 18.8° 2θ, but the identification of this phase was doubtful.

Due to the extraordinary complexity of the refinement project, not least due to the large number of phases, many of the refined parameters did not converge to a stable solution and had to be limited manually (Table 12). The fit obtained by the Rietveld refinement was still of high quality (Fig. 8) and showed almost no residual signal above the noise amplitude in the difference curve. However, several problematic trends were observed during the refinement process. The strong bending of the background curve between 10° and 15° 2θ in combination with the group of phyllosilicate peaks around 10° 2θ was problematic to fit with a polynomial function. The closest fit was obtained with 9 polynomial coefficients, which was the number automatically selected by BGMN. Functions with a lower number of coefficients were not flexible enough to model the bending, whereas a higher number of coefficients resulted in unstable background refinement at very low angles (<12° 2θ) and in the region from 25° to 35° 2θ. The strong correlations between peak data and the background polynomial at 25°–35° 2θ was the result of excessive peak overlap, particularly after adding the smectite structure with its strongly asymmetric intensities. Manually limiting the peak width parameter of several phases was necessary to obtain a stable solution. The signals of biotite, muscovite, and pyrophyllite were almost only defined by their 001 basal peaks around 10° 2θ. All other peaks were broad, weak, and overlapped with other phases. Therefore, only the *c* parameter could be refined for the phyllosilicates, whereas manual limits had to be set for the *a* and *b* axes.

The refinement statistics (Table 13) indicate a good quality of fit, but also expose the excessive number of peaks, more than half of which originate from the complex disordered smectite structure model. Refined phase quantities are reported for all phases, as well as for all phases excluding the phyllosilicates (Table 14). This allows direct comparison with the quantities reported in the ODR database, which also separated the quantification of poorly crystalline clay phases from all other crystalline phases. Bristow et al. (2021) hypothesized that talc-serpentine intergrades formed due to brine-driven destruction of phyllosilicates. Since talc and pyrophyllite are endmembers of a solid solution, structurally closely related, and exhibit an iconic *d*(001) peak at 9.45° and 9.62° 2θ, respectively, we found our identification to be in general agreement with the findings of Bristow et al. Approximately 53 wt% of the sample were composed of plagioclase feldspar and pyroxene, and another 30 wt% of the phyllosilicates. The sulphates accounted for about 7 wt%, and the remaining 9 wt% were relatively evenly distributed on quartz, goethite, and siderite. In large parts our refined phase quantities agree well with the results reported in the ODR database, but minor

Table 12

Refinement strategy for the “Mary Anning 3” dataset. Isotropically refined parameters are marked with “+”, fixed ones with “0”. Anisotropically refined parameters are marked with “++”. Preferred orientation refined with a spherical harmonics function is marked with “SPHARn”, where n stands for the order of the function. If a parameter did not converge to a minimum and was blocked by a manually set limit, it is marked by parentheses “()”. “Atomic sites” refers to site occupancies (“Occ.”), fractional coordinates, and thermal displacement parameters.

Phase	Cell parameters	Scale factor	Crystallite size	Micro-strain	Preferred orientation	Atomic sites
Plagioclase	+	+	+	+	SPHAR4	0
Pigeonite	+	+	(+)	0	0	0
Quartz	+	+	+	0	0	0
Goethite	+	+	(+)	0	0	0
Siderite	+	+	+	0	0	0
Anhydrite	+	+	(+)	0	0	0
Bassanite	+	+	+	0	0	0
Rozenite	(+)	+	(+)	0	0	0
Pyrophyllite	(+)	+	(+)	0	0	0
Biotite	(+)	+	(+)	0	0	0
Muscovite	(+)	+	(+)	0	0	0
Smectite	+	+	+	+	0	Occ.

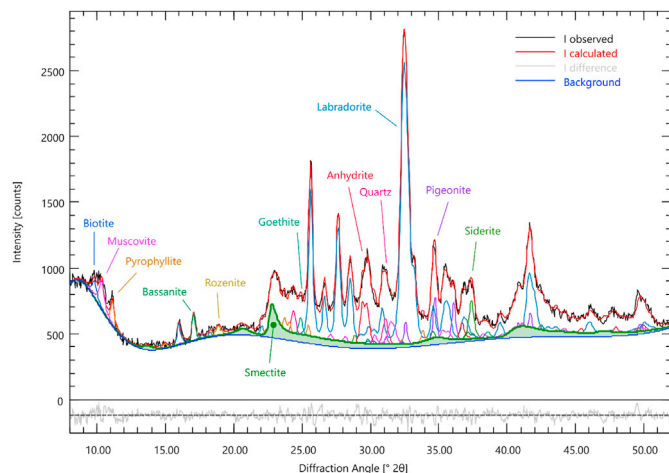


Fig. 8. Refinement of the “Mary Anning 3” sample. Iconic peaks of each phase are labelled. The pattern of the turbostratically disordered smectite structure is filled for better visibility.

Table 13

Goodness of fit and refinement statistics of the “Mary Anning 3” Rietveld refinement.

Parameter	Value
R_{wp}	3.95%
R_{exp}	3.45%
χ^2	1.31
Number of refined peaks	1032 (493 without smectite)
Number of refined parameters	99
Number of background coefficients	9

differences existed in the identified phases. We did not detect sanidine and hematite, but instead found goethite and rozenite, with the identification of the latter being doubtful. The sum of all phyllosilicates agreed surprisingly well with the sum of clay minerals reported in the ODR.

4. Discussion

The example refinements presented above focused on phase identification and quantification. The good pattern fits resulting in almost no residual signals exceeding the noise pattern demonstrated that the CheMin instrument configuration for *Profex* presented in this study is applicable in practice. The Mars Mineral Compendium, combined with the default structure repositories included in *Profex*, contained all phases necessary to process the CheMin datasets we retrieved from the ODR

Table 14

Refined phase quantities of the “Mary Anning 3” sample in relative wt.%. Errors of sample quantities represent twice the estimated standard deviations (2 ESD) reported by BGMN. Quantities normalized to the sum of all non-phyllosilicate phases (“without phyllosilicates”) are reported for easier comparison with quantities given in the ODR database. Values below 3-sigma are shown in parentheses.

Phase	“Mary Anning 3”		ODR
	<i>Profex</i>		
	All phases	Without phyllosilicates	
Plagioclase	45.9 ± 1.8	66.0 ± 2.6	63.7 ± 2.8
Sanidine	–	–	6.3 ± 3.2
Pigeonite	7.1 ± 0.7	10.2 ± 1.0	13.9 ± 5.7
Quartz	3.6 ± 0.7	5.2 ± 1.1	2.3 ± 1.0
Goethite	2.4 ± 0.4	3.5 ± 0.5	–
Siderite	3.1 ± 0.5	4.4 ± 0.8	(2.5 ± 1.7)
Anhydrite	3.8 ± 0.3	5.5 ± 0.4	4.6 ± 1.2
Bassanite	1.6 ± 0.3	2.3 ± 0.4	4.8 ± 0.5
Rozenite	2.0 ± 0.4	2.9 ± 0.6	–
Pyrophyllite	4.5 ± 0.8	+30.6 ± 2.6	+30.0 ± 11
Biotite	2.9 ± 0.6		
Muscovite	9.5 ± 1.0		
Smectite	13.7 ± 2.2		
Amorphous	–	–	+ (25.0 ± 19)

database. The example refinements covered a range of complexities from the relatively simple “Buckskin” to the complex “Mary Anning 3” samples. The identified phases were plausible and in general agreement with the compositions published in the ODR database. Differences occurred when phases were close to the detection limit of 1 wt%, poorly crystalline, or strongly overlapped by other signals, in other words when identification was ambiguous.

The angular resolution of CheMin is lower compared to high-resolution XRD instruments. This, in combination with the complex phase composition of the example datasets, resulted in strong peak overlap. As a consequence, the refined phase fractions may be strongly influenced by the adopted refinement strategy. For example, changing the model used to refine the preferred orientation can cause the scaling of superimposed peaks to change significantly. An example of pronounced overlap found in the “Rocknest” 4th scoop example is shown in Fig. 9. Peaks of augite, labradorite, pigeonite and forsterite overlap and are in sum only recognizable as a single measured peak. By refining preferred orientation, these phases are given additional degrees of freedom to adjust peak intensity independently of phase fraction. Since there is no unique solution for fitting a single measured peak by 4 freely scalable peak functions, the system is highly underdetermined and the calculated phase fractions are random. Such dependencies on the refinement strategy are most likely the cause of the sometimes strong differences

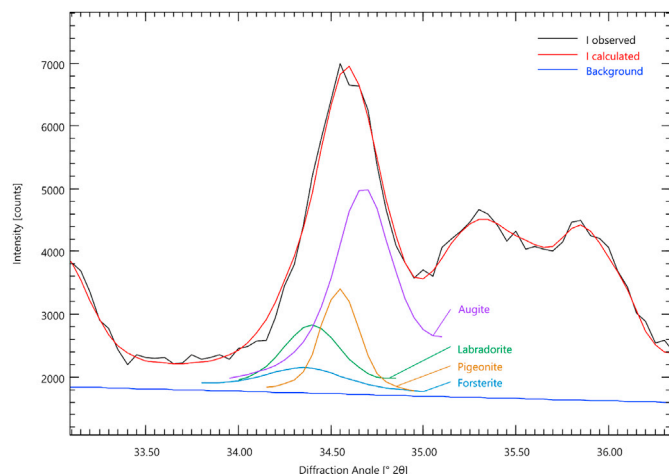


Fig. 9. The limited peak resolution and complex phase composition often leads to severe peak overlap, as demonstrated by the “Rocknest” 4th scoop refinement.

between the phase fractions calculated by *Profex* and the ODR. In our examples, we specifically tried to achieve stable refinements by minimizing the number of free parameters. An essential aspect of this was the omission of refinement of preferred orientation, micro-strain, and anisotropic crystallite sizes for poorly defined phases. This strategy was also supported by the fact that CheMin’s transmission cell makes alignment of the crystals very unlikely, especially since the samples are kept in convection by sonication.

Despite the recommendation to disable refinement of preferred orientation, we mentioned in the descriptions of the refinement strategies that it was enabled for phases exceeding 20 wt%. The reason is again found in the chemical variability of the feldspar and pyroxene systems. A structure model that does not represent the measured phase perfectly in terms of chemical composition not only differs in terms of peak positions, but also in peak intensities. The crystallographically correct way to address these intensity mismatches would be the refinement of atomic site parameters, such as site occupancy factors and fractional coordinates. However, we deemed the resolution, signal-to-noise ratio, and complexity of the CheMin datasets to be unsuitable for such advanced structure refinements. Instead we decided to enable refinement of preferred orientation using a low order of spherical harmonics (second or fourth order) for phases with a well-defined pattern, provided these phases did not exhibit severe peak overlap among each other. In relation to our previous example, this means that if only one of the phases depicted in Fig. 9 had preferred orientation enabled, there would still be a stable solution to fit the measured peak. Although this workaround was most likely not justified by the true sample properties and resulted in biased phase quantities, the improved fit of strong signals also improved the fit, and thus the quantification, of weaker signals.

Refinement of the background of the “John Klein” and “Mary Anning 3” datasets proved to be challenging due to a sharp increase below 14° 2θ (Figs. 6 and 8), which did not occur in the “Rocknest” and “Buckskin” datasets (Figs. 5 and 7). This background profile required a flexible polynomial to fit the abrupt rise, but a flexible polynomial risked unstable background modelling at higher angles. In comparisons with manually chosen polynomials, the automatic choice of coefficients by the BGMN refinement kernel was found to be a good compromise between the required flexibility at low angles, and stability at higher angles. Nevertheless, in samples “John Klein” and “Mary Anning 3”, wavelike background polynomials indicated a certain instability that may affect the accuracy of the phase quantifications.

Unstable refinements due to over-processing are sometimes difficult to spot because the pattern fit is often of high quality, which somewhat obscures the fact that parameters correlate and the results are unreliable. In Table 15 we summarized the general strategy we followed when

Table 15

Recommended refinement strategy, assuming that all phases have been identified and added to the refinement project.

Step	Action	Control file parameter
1	In the refinement control file (*.sav): Disable refinement of zero-shift, sample displacement, and sample transparency	EPS1 = 0 EPS2 = 0 EPS3 = 0
2	In all structure files (*.str): Disable refinement of preferred orientation, Disable refinement of micro-strain, Enable isotropic crystallite size refinement	GEWICHT = SPHAR0 k2 = 0, PARAM=B1=0_0^0.01
Run the refinement		
3	In the results file (*.lst): Examine the refined parameters, Values with a standard deviation reached a minimum, Values without standard deviation were blocked by a limit	A = 0.9876+0.0002 A = 0.9876
4	In the structure files (*.str): Increase the limits of blocked parameters	PARAM = A = 0.9900_0.9850^0.9950
Run the refinement		
5	In the structure files (*.str): If a parameter never converges and always reaches the limit, set the limit to a crystallographically reasonable value and leave it there. Consider replacing the structure with a better matching one, or removing it from the refinement.	
6	In the refinement graph (*.dia): Check if excessive peak broadening pushes the background polynomial towards the zero-line. If yes, limit peak broadening to a reasonable value. If unsure, set the limit to 0.01.	PARAM=B1=0_0^0.01
Run the refinement		
7	In the structure files (*.str): Enable ideal preferred orientation refinement for the strongest phase. Select the order based on the crystal morphology and cleavage. Check if the fit improves. If not, disable preferred orientation again.	GEWICHT = SPHAR4
Run the refinement		

processing examples 1 to 4. These steps avoided over-processing by starting with the lowest number of refined parameters required, and carefully releasing them for refinement as needed. The descriptions of our refinement strategy and example refinements are provided here to assist *Profex* users in obtaining high-quality and stable refinements of CheMin datasets.

The *Profex* software suite with the Rietveld refinement kernel *BGMN*, the new CheMin instrument configuration, and the Mars Mineral Compendium is distributed as open-source software for all major operating systems. This *Profex* solution is capable of processing CheMin datasets to identify and quantify phases in Martian soil and rock samples. This work also laid the foundation for use in future planetary exploration missions (Blake et al., 2021), for example with the upcoming generations CheMinX for exploration of Mars (Rampe et al., 2021) and CheMin-V for exploration of Venus (Blake et al., 2020).

5. Conclusion

We adapted the Rietveld refinement software *Profex* to the CheMin X-ray diffractometer onboard the Mars rover *Curiosity* by creating an instrument configuration file for the CheMin instrument setup. Successful application of the new configuration was demonstrated by refining 7 original datasets of Martian rock samples analyzed by CheMin. The Mars Mineral Compendium containing 241 ready-to-use structure models specifically selected for analysis of extraterrestrial rock samples was included in the *Profex* distribution packages. Combined with the new CheMin instrument template and the Mars Mineral Compendium, *Profex* is no longer limited to processing XRD datasets from earthbound

instruments, but also suitable for data acquired by CheMin on Mars, and possibly for successor generations for planetary, lunar, or asteroid exploration. Thanks to a liberal open-source license (GPL v2 or newer) and platform-independence, *Profex* provides a complete solution for the quantitative evaluation of CheMin XRD datasets that can be used without any restrictions by students as well as academic, industrial, and government professionals alike.

Author statement

Nicola Döbelin: Conceptualization, Methodology, Software, Formal analysis, Data Curation, Writing – Original Draft, Writing – Review & Editing, Visualization.

Richard Archer: Conceptualization, Investigation, Resources.

Valerie Tu: Conceptualization, Writing – Original Draft, Supervision, Project administration.

Declaration of competing interest

The authors declare that they have no known competing financial interests or personal relationships that could have appeared to influence the work reported in this paper.

Data availability

Links to our data are given in the acknowledgements of the manuscript

Acknowledgements

We would like to thank Dr. Douglas W. Ming for compiling CIF files for the Mars Mineral Compendium, and to the CheMin instrument team and MSL rover team for their contributions to the collection and analysis of the data utilized for this demonstration. The instrument configuration for CheMin named “NASA-Curiosity-CheMin” is included in the Profex distribution bundles version 5.1.0 and later. All refinement projects presented in this study are available for download on the “Tutorials” page of the Profex website (Doebelin, 2022).

References

- Bergmann, J., Friedel, P., Kleeberg, R., 2000. Handling of unusual instrumental profiles by the BGMN Rietveld program. *Mater. Sci. Forum* 321–324, 192–197. <https://doi.org/10.4028/www.scientific.net/msf.321-324.192>.
- Bergmann, J., Friedel, P., Kleeberg, R., 1998. BGMN - a new fundamental parameters based Rietveld program for laboratory X-ray sources, it's use in quantitative analysis and structure investigations. *IUCr Comm. Powder Diff. Newsl.* 20, 5–8.
- Blake, D., Hazen, R.M., Morrison, S.M., Bristow, T.S., Sarrazin, P., Zacny, K., Rampe, E.B., Downs, R.T., Yen, A., Ming, D.W., Morris, R.V., Vaniman, D., Treiman, A., Achilles, C.N., Craig, P.I., Marais, D.J., Des, Tu, V., Castle, N., Thorpe, M.T., 2021. In-situ crystallographic investigations of solar systems in the next decade. *Bull. AAS* 53. <https://doi.org/10.3847/25c2cfbc.c5ef6bc2>.
- Blake, D., Vaniman, D., Achilles, C., Anderson, R., Bish, D., Bristow, T., Chen, C., Chipera, S., Crisp, J., Des Marais, D., Downs, R.T., Farmer, J., Feldman, S., Fonda, M., Gailhanou, M., Ma, H., Ming, D.W., Morris, R.V., Sarrazin, P., Stolper, E., Treiman, A., Yen, A., 2012. Characterization and calibration of the CheMin mineralogical instrument on Mars science laboratory. *Space Sci. Rev.* 170, 341–399. <https://doi.org/10.1007/s11214-012-9905-1>.
- Blake, D.F., Sarrazin, P., Bristow, T., Walroth, R., Downs, R., Yen, A., Zacny, K., 2020. CheMin-V: a definitive mineralogy instrument for landed science on Venus. In: *VEXAG Venus Exploration Analysis Group*, pp. 1–2.
- Bristow, T.F., Grotzinger, J.P., Rampe, E.B., Cuadros, J., Chipera, S.J., Downs, G.W., Fedo, C.M., Frydenvang, J., McAdam, A.C., Morris, R.V., Achilles, C.N., Blake, D.F., Castle, N., Craig, P., Des Marais, D.J., Downs, R.T., Hazen, R.M., Ming, D.W., Morrison, S.M., Thorpe, M.T., Treiman, A.H., Tu, V., Vaniman, D.T., Yen, A.S., Gellert, R., Mahaffy, P.R., Wiens, R.C., Bryk, A.B., Bennett, K.A., Fox, V.K., Milliken, R.E., Fraeman, A.A., Vasavada, A.R., 2021. Brine-driven destruction of clay minerals in Gale crater, Mars. *Science* (80-) 373, 198–204. <https://doi.org/10.1126/science.abg5449>.
- Bristow, T.F., Rampe, E.B., Achilles, C.N., Blake, D.F., Chipera, S.J., Craig, P., Crisp, J.A., Des Marais, D.J., Downs, R.T., Gellert, R., Grotzinger, J.P., Gupta, S., Hazen, R.M., Horgan, B., Hoggan, J.V., Mangold, N., Mahaffy, P.R., McAdam, A.C., Ming, D.W., Morokian, J.M., Morris, R.V., Morrison, S.M., Treiman, A.H., Vaniman, D.T., Vasavada, A.R., Yen, A.S., 2018. Clay mineral diversity and abundance in sedimentary rocks of Gale crater, Mars. *Sci. Adv.* 4. <https://doi.org/10.1126/sciadv.aar3330>.
- Chipera, S.J., Bish, D.L., 2002. FULLPAT : a full-pattern quantitative analysis program for X-ray powder diffraction using measured and calculated patterns. *J. Appl. Crystallogr.* 35, 744–749. <https://doi.org/10.1107/S0021889802017405>.
- Doebelin, N., 2022. Profex - Open Source XRD and Rietveld Refinement [WWW Document]. <https://www.profex-xrd.org>.
- Doebelin, N., Kleeberg, R., 2015. Profex: a graphical user interface for the Rietveld refinement program BGMN. *J. Appl. Crystallogr.* 48, 1573–1580. <https://doi.org/10.1107/S1600576715014685>.
- Fraeman, A.A., Edgar, L.A., Rampe, E.B., Thompson, L.M., Frydenvang, J., Fedo, C.M., Catalano, J.G., Dietrich, W.E., Gabriel, T.S.J., Vasavada, A.R., Grotzinger, J.P., L'Haron, J., Mangold, N., Sun, V.Z., House, C.H., Bryk, A.B., Hardgrove, C., Czarnecki, S., Stack, K.M., Morris, R.V., Arvidson, R.E., Banham, S.G., Bennett, K.A., Bridges, J.C., Edwards, C.S., Fischer, W.W., Fox, V.K., Gupta, S., Horgan, B.H.N., Jacob, S.R., Johnson, J.R., Johnson, S.S., Rubin, D.M., Salvatore, M.R., Schwenzer, S.P., Siebach, K.L., Stein, N.T., Turner, S.M.R., Wellington, D.F., Wiens, R.C., Williams, A.J., David, G., Wong, G.M., 2020. Evidence for a diagenetic origin of Vera Rubin ridge, Gale crater, Mars: summary and synthesis of curiosity's exploration campaign. *J. Geophys. Res. Planets* 125. <https://doi.org/10.1029/2020JE006527>, 2020.
- Grotzinger, J.P., Sumner, D.Y., Kah, L.C., Stack, K., Gupta, S., Edgar, L., Rubin, D., Lewis, K., Schieber, J., Mangold, N., Milliken, R., Conrad, P.G., DesMarais, D., Farmer, J., Siebach, K., Calef, F., Hurowitz, J., McLennan, S.M., Ming, D., Vaniman, D., Crisp, J., Vasavada, A., Edgett, K.S., Malin, M., Blake, D., Gellert, R., Mahaffy, P., Wiens, R.C., Maurice, S., Grant, J.A., Wilson, S., Anderson, R.C., Beegle, L., Arvidson, R., Hallet, B., Sletten, R.S., Rice, M., Bell, J., Griffes, J., Ehlmann, B., Anderson, R.B., Bristow, T.F., Dietrich, W.E., Dromart, G., Eigenbrode, J., Fraeman, A., Hardgrove, C., Herkenhoff, K., Jandura, L., Kocurek, G., Lee, S., Leshin, L.A., Leveille, R., Limonadi, D., Maki, J., McCloskey, S., Meyer, M., Minitti, M., Newsom, H., Oehler, D., Okon, A., Palucis, M., Parker, T., Rowland, S., Schmidt, M., Squyres, S., Steele, A., Stolper, E., Summons, R., Treiman, A., Williams, R., Yingst, A., Team, M.S., Kemppinen, O., Bridges, N., Johnson, J.R., Cremers, D., Godber, A., Wadhwa, M., Wellington, D., McEwan, I., Newman, C., Richardson, M., Charpentier, A., Peret, L., King, P., Blank, J., Weigle, G., Li, S., Robertson, K., Sun, V., Baker, M., Edwards, C., Farley, K., Miller, H., Newcombe, M., Pilorget, C., Brunet, C., Hipkin, V., Léveillé, R., Marchand, G., Sánchez, P.S., Favot, L., Cody, G., Flückiger, L., Lees, D., Nefian, A., Martin, M., Gailhanou, M., Westall, F., Israël, G., Agard, C., Baroukh, J., Donny, C., Gaboriaud, A., Guillemot, P., Lafaille, V., Lorigny, E., Paillet, A., Pérez, R., Saccoccio, M., Yana, C., Armiens-Aparicio, C., Rodríguez, J.C., Blázquez, I.C., Gómez, F.G., Gómez-Elvira, J., Hettrich, S., Malvitte, A.L., Jiménez, M.M., Martínez-Frías, J., Martín-Soler, J., Martín-Torres, F.J., Jurado, A.M., Mora-Sotomayor, L., Caro, G.M., López, S.N., Peinado-González, V., Pla-García, J., Manfredi, J.A.R., Romeral-Planelló, J.J., Fuentes, S.A.S., Martínez, E.S., Redondo, J.T., Urqui-O'Callaghan, R., Mier, M.-P.Z., Chipera, S., Lacour, J.-L., Mauchien, P., Sirven, J.-B., Manning, H., Fairén, A., Hayes, A., Joseph, J., Sullivan, R., Thomas, P., Dupont, A., Lundberg, A., Melikechi, N., Mezzacappa, A., DeMarines, J., Grinspoon, D., Reitz, G., Prats, B., Atlaskin, E., Genzer, M., Harri, A.-M., Haukka, H., Kahanpää, H., Kahanen, J., Paton, M., Polkko, J., Schmidt, W., Siili, T., Fabre, C., Wray, J., Wilhelm, M.B., Poitrasson, F., Patel, K., Gorevan, S., Indyk, S., Paulsen, G., Bish, D., Gondet, B., Langevin, Y., Geoffroy, C., Baratoux, D., Berger, G., Cros, A., D'Uston, C., Forni, O., Gasnault, O., Lasue, J., Lee, Q.-M., Meslin, P.-Y., Pallier, E., Parot, Y., Pinet, P., Schröder, S., Toplis, M., Lewin, É., Brunner, W., Heydari, E., Achilles, C., Sutter, B., Cabane, M., Coscia, D., Szopa, C., Robert, F., Sautter, V., Le Mouélic, S., Nachon, M., Buch, A., Stalport, F., Coll, P., François, P., Raulin, F., Teinturier, S., Cameron, J., Clegg, S., Cousin, A., DeLapp, D., Dingler, R., Jackson, R.S., Johnstone, S., Lanza, N., Little, C., Nelson, T., Williams, R.B., Jones, A., Kirkland, L., Baker, B., Cantor, B., Caplinger, M., Davis, S., Daston, B., Fay, D., Harker, D., Herrera, P., Jensen, E., Kennedy, M.R., Krezoski, G., Krysak, D., Lipkaman, L., McCartney, E., McNair, S., Nixon, B., Posiolova, L., Ravine, M., Salamon, A., Saper, L., Stoiber, K., Supulver, K., Van Beek, J., Van Beek, T., Zimdar, R., French, K.L., Iagnemma, K., Miller, K., Goessmann, F., Goetz, W., Hvuid, S., Johnson, M., Lefavor, M., Lyness, E., Breves, E., Dyar, M.D., Fassett, C., Edwards, L., Haberle, R., Hoehler, T., Hollingsworth, J., Kahre, M., Keely, L., McKay, C., Bleacher, L., Brinckerhoff, W., Choi, D., Dworkin, J.P., Floyd, M., Freissinet, C., Garvin, J., Glavin, D., Harpold, D., Martin, D.K., McAdam, A., Pavlov, A., Raaen, E., Smith, M.D., Stern, J., Tan, F., Trainer, M., Posner, A., Voytek, M., Aubrey, A., Behar, A., Blaney, D., Brinza, D., Christensen, L., DeFlores, L., Feldman, J., Feldman, S., Flesch, G., Jun, I., Keymeulen, D., Mischna, M., Morokian, J.M., Pavri, B., Schoppers, M., Sengstacken, A., Simmonds, J.J., Spanovich, N., Juarez, M. de la T., Webster, C.R., Yen, A., Archer, P.D., Cucinotta, F., Jones, J.H., Morris, R.V., Niles, P., Rampe, E., Nolan, T., Fisk, M., Radziemski, L., Barraclough, B., Bender, S., Berman, D., Dobre, E.N., Tokar, R., Clegghorn, T., Huntress, W., Manhès, G., Hudgins, J., Olson, T., Stewart, N., Sarrazin, P., Vicenzi, E., Bullock, M., Ehresmann, B., Hamilton, V., Hassler, D., Peterson, J., Rafkin, S., Zeitlin, C., Fedosov, F., Golovin, D., Karpushkina, N., Kozlyev, A., Litvak, M., Malakhov, A., Mitrofanov, I., Mokrousov, M., Nikiforov, S., Prokhorov, V., Sanin, A., Tretyakov, V., Varenikov, A., Vostrukhin, A., Kuzmin, R., Clark, B., Wolff, M., Botta, O., Drake, D., Bean, K., Lemmon, M., Schwenzer, S.P., Lee, E.M., Sucharski, R., Hernández, M.A. de P., Ávalos, J.J.B., Ramos, M., Kim, M.-H., Malespin, C., Plante, I., Müller, J.-P., Navarro-González, R., Ewing, R., Boynton, W., Downs, R., Fitzgibbon, M., Harshman, K., Morrison, S., Kortmann, O., Williams, A., Lugmair, G., Wilson, M.A., Jakosky, B., Balic-Zunic, T., Frydenvang, J., Jensen, J.K., Kinch, K., Koefoed, A., Madsen, M.B., Stipp, S.L.S., Boyd, N., Campbell, J.L., Perrett, G., Pradler, I., VanBommel, S., Jacob, S., Owen, T., Savijärvi, H., Boehm, E., Böttcher, S.,

- Burmeister, S., Guo, J., Köhler, J., García, C.M., Mueller-Mellin, R., Wimmer-Schweingruber, R., Bridges, J.C., McConnochie, T., Benna, M., Franz, H., Bower, H., Brunner, A., Blau, H., Boucher, T., Carnosino, M., Atreya, S., Elliott, H., Halleaux, D., Rennó, N., Wong, M., Pepin, R., Elliott, B., Spray, J., Thompson, L., Gordon, S., Ollila, A., Williams, J., Vasconcelos, P., Bentz, J., Neelson, K., Popa, R., Moersch, J., Tate, C., Day, M., Francis, R., McCullough, E., Cloutis, E., ten Kate, I.L., Scholes, D., Slavney, S., Stein, T., Ward, J., Berger, J., Moores, J.E., 2014. A habitable fluvio-lacustrine environment at Yellowknife Bay, Gale crater, Mars. *Science* (80-) 343. <https://doi.org/10.1126/science.1242777>.
- Hölzer, G., Fritsch, M., Deutsch, M., Härtwig, J., Förster, E., 1997. $K\alpha_{1,2}$ and $K\beta_{1,3}$ x-ray emission lines of the 3d transition metals. *Phys. Rev. A* 56, 4554–4568.
- Hurowitz, J.A., Grotzinger, J.P., Fischer, W.W., McLennan, S.M., Milliken, R.E., Stein, N., Vasavada, A.R., Blake, D.F., Dehouck, E., Eigenbrode, J.L., Fairén, A.G., Frydenvang, J., Gellert, R., Grant, J.A., Gupta, S., Herkenhoff, K.E., Ming, D.W., Rampe, E.B., Schmidt, M.E., Siebach, K.L., Stack-Morgan, K., Sumner, D.Y., Wiens, R.C., 2017. Redox stratification of an ancient lake in Gale crater, Mars. *Science* (80-) 356. <https://doi.org/10.1126/science.aah6849>.
- IUCr, 2022. Crystallographic Software List [WWW Document]. <https://www.iucr.org/resources/other-directories/software>.
- Madsen, I.C., Scarlett, N.V.Y., 2008. Quantitative phase Analysis. In: Dinnebier, R.E., Billinge, S.J.L. (Eds.), *Powder Diffraction: Theory and Practice*. The Royal Society of Chemistry, Cambridge, pp. 298–331. <https://doi.org/10.1039/9781847558237-00298>.
- Martin, P.E., Farley, K.A., Baker, M.B., Malespin, C.A., Schwenzer, S.P., Cohen, B.A., Mahaffy, P.R., McAdam, A.C., Ming, D.W., Vasconcelos, P.M., Navarro-González, R., 2017. A two-step K-Ar experiment on Mars: dating the diagenetic formation of jarosite from amazonian groundwaters. *J. Geophys. Res. Planets* 122, 2803–2818. <https://doi.org/10.1002/2017JE005445>.
- Morris, R.V., Vaniman, D.T., Blake, D.F., Gellert, R., Chipera, S.J., Rampe, E.B., Ming, D.W., Morrison, S.M., Downs, R.T., Treiman, A.H., Yen, A.S., Grotzinger, J.P., Achilles, C.N., Bristow, T.F., Crisp, J.A., Des Marais, D.J., Farmer, J.D., Fendrich, K.V., Frydenvang, J., Graff, T.G., Morookian, J.-M., Stolper, E.M., Schwenzer, S.P., 2016. Silicic volcanism on Mars evidenced by tridymite in high-SiO₂ sedimentary rock at Gale crater. *Proc. Natl. Acad. Sci. USA* 113, 7071–7076. <https://doi.org/10.1073/pnas.1607098113>.
- Morrison, S.M., Downs, R.T., Blake, D.F., Vaniman, D.T., Ming, D.W., Hazen, R.M., Treiman, A.H., Achilles, C.N., Yen, A.S., Morris, R.V., Rampe, E.B., Bristow, T.F., Chipera, S.J., Sarrazin, P.C., Gellert, R., Fendrich, K.V., Morookian, J.M., Farmer, J.D., Des Marais, D.J., Craig, P.I., 2018. Crystal chemistry of martian minerals from Bradbury landing through Naukluft plateau, Gale Crater, Mars. *Am. Mineral.* 103, 857–871. <https://doi.org/10.2138/am-2018-6124>.
- Open Data Repository, 2022. Chemin Database [WWW Document]. <https://odr.io/chemin>.
- Payré, V., Siebach, K.L., Thorpe, M.T., Antoshechkina, P., Rampe, E.B., 2022. Tridymite in a lacustrine mudstone in Gale crater, Mars: evidence for an explosive silicic eruption during the Hesperian. *Earth Planet Sci. Lett.* 594, 117694. <https://doi.org/10.1016/j.epsl.2022.117694>.
- Peretyazhko, T.S., Fox, A., Sutter, B., Niles, P.B., Adams, M., Morris, R.V., Ming, D.W., 2016. Synthesis of akaganeite in the presence of sulfate: implications for akaganeite formation in Yellowknife Bay, Gale crater, Mars. *Geochim. Cosmochim. Acta* 188, 284–296. <https://doi.org/10.1016/j.gca.2016.06.002>.
- Rampe, E., Blake, D., Sarrazin, P., Bristow, T., Gailhanou, M., Lafuente, B., Tu, V., Zaczyn, K., Downs, R., 2021. CheMinX: a next generation XRD/XRF for quantitative mineralogy and geochemistry on Mars. *Bull. AAS* 53. <https://doi.org/10.3847/252c2feb.a4a55445>.
- Rampe, E.B., Blake, D.F., Bristow, T.F., Ming, D.W., Vaniman, D.T., Morris, R.V., Achilles, C.N., Chipera, S.J., Morrison, S.M., Tu, V.M., Yen, A.S., Castle, N., Downs, G.W., Downs, R.T., Grotzinger, J.P., Hazen, R.M., Treiman, A.H., Peretyazhko, T.S., Des Marais, D.J., Walroth, R.C., Craig, P., Crisp, J.A., Lafuente, B., Morookian, J.M., Sarrazin, P.C., Thorpe, M.T., Bridges, J.C., Edgar, L.A., Fedo, C.M., Freissinet, C., Gellert, R., Mahaffy, P.R., Newsom, H.E., Johnson, J.R., Kah, L.C., Siebach, K.L., Schieber, J., Sun, V.Z., Vasavada, A.R., Wellington, D., Wiens, R.C., 2020. Mineralogy and geochemistry of sedimentary rocks and eolian sediments in Gale crater, Mars: a review after six Earth years of exploration with Curiosity. *Geochemistry* 80, 125605. <https://doi.org/10.1016/j.chemer.2020.125605>.
- Rampe, E.B., Bristow, T.F., Morris, R.V., Morrison, S.M., Achilles, C.N., Ming, D.W., Vaniman, D.T., Blake, D.F., Tu, V.M., Chipera, S.J., Yen, A.S., Peretyazhko, T.S., Downs, R.T., Hazen, R.M., Treiman, A.H., Grotzinger, J.P., Castle, N., Craig, P.I., Des Marais, D.J., Thorpe, M.T., Walroth, R.C., Downs, G.W., Fraeman, A.A., Siebach, K.L., Gellert, R., Lafuente, B., McAdam, A.C., Meslin, P.Y., Sutter, B., Salvatore, M.R., 2020. Mineralogy of Vera Rubin ridge from the Mars science laboratory CheMin instrument. *J. Geophys. Res. Planets* 125. <https://doi.org/10.1029/2019JE006306>.
- Rampe, E.B., Ming, D.W., Blake, D.F., Bristow, T.F., Chipera, S.J., Grotzinger, J.P., Morris, R.V., Morrison, S.M., Vaniman, D.T., Yen, A.S., Achilles, C.N., Craig, P.I., Des Marais, D.J., Downs, R.T., Farmer, J.D., Fendrich, K.V., Gellert, R., Hazen, R.M., Kah, L.C., Morookian, J.M., Peretyazhko, T.S., Sarrazin, P., Treiman, A.H., Berger, J.A., Eigenbrode, J., Fairén, A.G., Forni, O., Gupta, S., Hurowitz, J.A., Lanza, N.L., Schmidt, M.E., Siebach, K., Sutter, B., Thompson, L.M., 2017. Mineralogy of an ancient lacustrine mudstone succession from the Murray formation, Gale crater, Mars. *Earth Planet Sci. Lett.* 471, 172–185. <https://doi.org/10.1016/j.epsl.2017.04.021>.
- Rampe, E.B., Morris, R.V., Archer, P.D., Agresti, D.G., Ming, D.W., 2016. Recognizing sulfate and phosphate complexes chemisorbed onto nanophase weathering products on Mars using in-situ and remote observation sk. *Am. Mineral.* 101, 678–689. <https://doi.org/10.2138/am-2016-5408CCBYNCND>.
- Rietveld, H.M., 1969. A profile refinement method for nuclear and magnetic structures. *J. Appl. Crystallogr.* 2, 65.
- Tu, V.M., Rampe, E.B., Bristow, T.F., Thorpe, M.T., Clark, J.V., Castle, N., Fraeman, A.A., Edgar, L.A., McAdam, A., Bedford, C., Achilles, C.N., Blake, D., Chipera, S.J., Craig, P.I., Des Marais, D.J., Downs, G.W., Downs, R.T., Fox, V., Grotzinger, J.P., Hazen, R.M., Ming, D.W., Morris, R.V., Morrison, S.M., Pavri, B., Eigenbrode, J., Peretyazhko, T.S., Sarrazin, P.C., Sutter, B., Treiman, A.H., Vaniman, D.T., Vasavada, A.R., Yen, A.S., Bridges, J.C., 2021. A review of the phyllosilicates in Gale crater as detected by the CheMin instrument on the Mars science laboratory, curiosity rover. *Minerals* 11, 847. <https://doi.org/10.3390/min11080847>.
- Ufer, K., Kleeberg, R., Bergmann, J., Curtius, H., Dohrmann, R., 2008. Refining real structure parameters of disordered layer structures within the rietveld method. *Zeitschrift für Krist (Suppl)*, 151–158. <https://doi.org/10.1524/zksu.2008.0020>.
- Vaniman, D.T., Bish, D.L., Ming, D.W., Bristow, T.F., Morris, R.V., Blake, D.F., Chipera, S.J., Morrison, S.M., Treiman, A.H., Rampe, E.B., Rice, M., Achilles, C.N., Grotzinger, J.P., McLennan, S.M., Williams, J., Bell, J.F., Newsom, H.E., Downs, R.T., Maurice, S., Sarrazin, P., Yen, A.S., Morookian, J.M., Farmer, J.D., Stack, K., Milliken, R.E., Ehlmann, B.L., Sumner, D.Y., Berger, G., Crisp, J.A., Hurowitz, J.A., Anderson, R., Des Marais, D.J., Stolper, E.M., Edgett, K.S., Gupta, S., Spanovich, N., Agard, C., Alves Verdasca, J.A., Anderson, Ryan, Archer, D., Armien-Aparicio, C., Arvidson, R., Atkinson, E., Atreya, S., Aubrey, A., Baker, B., Baker, M., Balic-Zunic, T., Baratoux, D., Baroukh, J., Barraclough, B., Bean, K., Beegle, L., Behar, A., Bender, S., Benna, M., Bentz, J., Berger, J., Berman, D., Blanco Avalos, J.J., Blaney, D., Blank, J., Blau, H., Bleacher, L., Boehm, E., Botta, O., Böttcher, S., Boucher, T., Bower, H., Boyd, N., Boynton, B., Breves, E., Bridges, J., Bridges, N., Brinkerhoff, W., Brinza, D., Brunet, C., Brunner, A., Brunner, W., Buch, A., Bullock, M., Burmeister, S., Cabane, M., Calef, F., Cameron, J., Campbell, J., Iain, Cantor, B., Caplinger, M., Caride Rodríguez, J., Carnosino, M., Carrasco Blázquez, I., Charpentier, A., Choi, D., Clark, B., Clegg, S., Cleghorn, T., Cloutis, E., Cody, G., Coll, P., Conrad, P., Coscia, D., Cousin, A., Cremers, D., Cros, A., Cucinotta, F., D'Uston, C., Davis, S., Day, M., Kenzie, de la Torre Juarez, M., DeFlores, L., DeLapp, D., DeMarines, J., Dietrich, W., Dingler, R., Donny, C., Drake, D., Dromart, G., Dupont, A., Duston, B., Dworkin, J., Dyr, M.D., Edgar, L., Edwards, C., Edwards, L., Ehresmann, B., Eigenbrode, J., Elliott, B., Elliott, H., Ewing, R., Fabre, C., Fairén, A., Farley, K., Fassett, C., Favot, L., Fay, D., Fedosov, F., Feldman, J., Feldman, S., Fisk, M., Fitzgibbon, M., Flesch, G., Floyd, M., Flückiger, L., Forni, O., Fraeman, A., Francis, R., François, P., Franz, H., Freissinet, C., French, K.L., Frydenvang, J., Gaboriaud, A., Gailhanou, M., Garvin, J., Gasnault, O., Goffroy, C., Gellert, R., Genzer, M., Glavin, D., Godber, A., Goeumont, F., Goetz, W., Golovin, D., Gómez Gómez, F., Gómez-Elvira, J., Gondet, B., Gordon, S., Gorevan, S., Grant, J., Griffes, J., Grinspoon, D., Guillemot, P., Guo, J., Guzewich, S., Haberle, R., Halleaux, D., Hallet, B., Hamilton, V., Hardgrove, C., Harker, D., Harpold, D., Harri, A.-M., Harshman, K., Hassler, D., Hauka, H., Hayes, A., Herkenhoff, K., Herrera, P., Hettich, S., Heydari, E., Hipkin, V., Hoehler, T., Hollingsworth, J., Hudgins, J., Huntress, W., Hviid, S., Iagnemma, K., Indyk, S., Israël, G., Jackson, R., Jacob, S., Jakosky, B., Jensen, E., Jensen, J.K., Johnson, J., Johnson, M., Johnstone, S., Jones, A., Jones, J., Joseph, J., Jun, I., Kah, L., Kahanpää, H., Kahre, M., Karpushkina, N., Kasprzak, W., Kauhaneen, J., Keely, L., Kempainen, O., Keymeulen, D., Kim, M.-H., Kinch, K., King, P., Kirkland, L., Kocurek, G., Koefoed, A., Köhler, J., Kortmann, O., Kozyrev, A., Krezoski, J., Krysak, D., Kuzmin, R., Lacour, J.L., Lafaille, V., Langevin, Y., Lanza, N., Lasue, J., Le Mouélic, S., Lee, E.M., Lee, Q.-M., Lees, D., Lefavre, M., Lemmon, M., Malville, A.L., Leshin, L., Léveillé, R., Lewin-Carpentier, E., Lewis, K., Li, S., Lipkaman, L., Little, C., Litvak, M., Lorigny, E., Lugmair, G., Lundberg, A., Lyness, E., Madsen, M., Mahaffy, P., Maki, J., Malakhov, A., Malespin, C., Malin, M., Mangold, N., Manhes, G., Manning, H., Marchand, G., Marín Jiménez, M., Martín García, C., Martin, D., Martin, M., Martínez-Frías, J., Martín-Soler, J., Martín-Torres, F.J., Mauchien, P., McAdam, A., McCartney, E., McConnochie, T., McCullough, E., McEwan, I., McKay, C., McNair, S., Melikechi, N., Meslin, P.-Y., Meyer, M., Mezzacappa, A., Miller, H., Miller, K., Minitti, M., Mischna, M., Mitrofanov, I., Moersch, J., Mokrousov, M., Molina Jurado, A., Moores, J., Mora-Sotomayor, L., Mueller-Mellin, R., Muller, J.-P., Muñoz Caro, G., Nachon, M., Navarro López, S., Navarro-González, R., Neelson, K., Nefian, A., Nelson, T., Newcombe, M., Newman, C., Nikiforov, S., Niles, P., Nixon, B., Noe Dobrea, E., Nolan, T., Oehler, D., Ollila, A., Olson, T., Owen, T., de Pablo Hernández, M.A., Paillet, A., Pallier, E., Palucis, M., Parker, T., Parot, Y., Patel, K., Paton, M., Paulsen, G., Pavlov, A., Pavri, B., Peinado-González, V., Pepin, R., Peret, L., Perez, R., Perrett, G., Peterson, J., Pilorget, C., Pinet, P., Pla-García, J., Plante, I., Poitrasson, F., Polko, J., Popa, R., Posilova, L., Posner, A., Pradler, I., Prats, B., Prokhorov, V., Purdy, S.W., Raaen, E., Radziemski, L., Rafkin, S., Ramos, M., Raulin, F., Ravine, M., Reitz, G., Rennó, N., Richardson, M., Robert, F., Robertson, K., Rodríguez Manfredi, J.A., Romeral-Planelló, J.J., Rowland, S., Rubin, D., Saccoccio, M., Salamon, A., Sandoval, J., Sanin, A., Sans Fuentes, S.A., Saper, L., Sautter, V., Savijärvi, H., Schieber, J., Schmidt, M., Schmidt, W., Scholes, D., Dan, Schoppers, M., Schröder, S., Schwenzer, S., Sebastian Martinez, E., Sengstacken, A., Shterts, R., Siebach, K., Siili, T., Simmonds, J., Sirven, J.-B., Slavney, S., Sletten, R., Smith, M., Sobrón Sánchez, P., Spray, J., Squyres, S., Stalport, F., Steele, A., Stein, T., Stern, J., Stewart, N., Stipp, S.L.S., Stoiber, K., Sucharski, B., Sullivan, R., Summons, R., Sun, V.,

Supulver, K., Sutter, B., Szopa, C., Tan, F., Tate, C., Teinturier, S., ten Kate, I., Thomas, P., Thompson, L., Tokar, R., Toplis, M., Torres Redondo, J., Trainer, M., Tretyakov, V., Urqui-O'Callaghan, R., Van Beek, J., Van Beek, T., VanBommel, S., Varenikov, A., Vasavada, A., Vasconcelos, P., Vicenzi, E., Vostrukhin, A., Voytek, M., Wadhwa, M., Ward, J., Webster, C., Weigle, E., Wellington, D., Westall, F.,

Wiens, R.C., Wilhelm, M.B., Williams, A., Williams, R., Williams, R.B., Mouser, Wilson, M., Wimmer-Schweingruber, R., Wolff, M., Wong, M., Wray, J., Wu, M., Yana, C., Yingst, A., Zeitlin, C., Zimdar, R., Zorzano Mier, M.-P., 2014. Mineralogy of a mudstone at Yellowknife Bay, Gale crater, Mars. *Science* (80-) 343. <https://doi.org/10.1126/science.1243480>.